Observations of Infrared Absorbance by the B_{2u} and B_{3u} Fundamentals of Rhombic Li_2F_2 Matrix Isolated in Xe and Ar†

Richard L. Redington*

Department of Chemistry and Biochemistry, Texas Tech University, Lubbock, Texas 79409

Received: April 25, 2009; Revised Manuscript Received: June 3, 2009

Infrared absorption spectra of the Li_2F_2 rhombic dimer isolated in Xe, Ar, and Ar-mixed matrices suggest that rotational stereodynamics occurs for Li_2F_2 in its Xe trapping site. Providing evidence for this, the absorbance peak for the B_{3u} fundamental at 617 cm^{-1} changes little upon annealing and heating processes, which cause the B_{2u} peak at 534 cm^{-1} to lose most of its absorbance strength—despite their common provenience. The explanation is rooted in (a) the volume compatibility of Li_2F_2 and the Xe vacancy, (b) the D_{2h} symmetry of Li_2F_2, (c) the state-specific generation of rotational stereodynamics by vibrational relaxation of the 534 cm^{-1} B_{2u} mode, and (d) the IR transparency manifested by Li_2F_2 isolated in Xe crystallites providing rough alignments between the B_{2u} transition dipole and the spectrometer IR beam. Analogous behavior appears to occur for the Xe-isolated LiF monomer.

1. Introduction

Properties of the gaseous molecules obtained by heating solid metal halides to high temperatures are of long-standing scientific interest,[1] and low temperature infrared matrix isolation (IRMI) studies of trapped LiF vapors[2−12] have revealed properties of the $(LiF)_{n=1-4}$ species. The 1998 review by Haas and Samuni[13] summarizes much knowledge concerning the nature of low temperature matrix deposits and trapping sites to show that even the simplest matrix systems are inherently complex. Nevertheless, simple intuitive approaches based on size and symmetry arguments can be informative concerning the diverse behaviors of atoms or small guest molecules isolated in rare gas (rg) solids. The potential energy surfaces (PESs) for some guest−host combinations, cf. rg-isolated HF,[14] H_2O,[15] NH_3,[16] and CH_4,[17] produce rich IR spectral observations involving rotational motions of the guest molecules in their trapping sites. IR fluorescence studies[18] suggest that nearly free rotation occurs for the CN radical in its Xe trapping site, and rotational behavior is believed to enter importantly into the vibrational relaxation mechanisms of rg-isolated CN. IR absorption can induce geometrical isomerizations of appropriate guest substances,[19] and early experiments (cf. N_2O_3 isolated[20] in N_2) simply utilized the spectrometer IR beam. In the present work, it is concluded that the vibrational relaxation process following the normal spectrometric excitation of the 534 cm^{-1} B_{2u} transition of Xe-isolated Li_2F_2 perpetrates rotational stereodynamics by Li_2F_2 in its Xe trapping site at an onset temperature above 4.2 K but below 20 K.

2. Procedures

The IR matrix isolation experiments were performed in the classical manner using a stainless steel cryostat furnished with a CsI sample deposition window cooled to a nominal 4.2 K by contact with a reservoir of liquid helium.[6] A beam of hot LiF vapor effused from an iron Knudsen cell at ca. 880 °C was codeposited with a stream of matrix gas onto the CsI cold window over a period of about 1.5 h. The matrix/sample ratio estimate M/LiF = 500 was used for the described experiments. In this work, the Ar and Xe trapping sites are discussed in terms of the 12 nearest-neighbor (nn) atoms surrounding the single-substitutional (ss) rg vacancy. The straightforward description accounts for the thermally induced changes of relative IR absorbance by transitions of LiF and Li_2F_2 isolated in Xe, Ar, and Ar-mixed matrix trapping sites.

3. IR Spectroscopic Results

Figure 1 presents IR absorption spectra observed for LiF vapor species isolated in a Xe matrix. The spectrum as deposited and recorded at 4.2 K appears in Figure 1A, with the most intense transitions due to monomer (823 cm^{-1}) and rhombic dimer (617 and 534 cm^{-1}). Figure 1B shows spectral changes generated by allowing the sample in Figure 1A to warm to ca. 20 K and then cooling it back to 4.2 K with liquid He. The B_{3u} rhombic dimer peak at 617 cm^{-1} survives this annealing process with minor changes in its peak maximum and bandwidth. The behavior for the B_{2u} dimer peak at 534 cm^{-1} is very different—despite the fact that the 617 and 534 cm^{-1} peaks both originate from the same sample of Xe-isolated Li_2F_2 rhombic dimer. In Figure 1A, the absorbance maximum at 534 cm^{-1} is slightly greater than that at 617 cm^{-1}. In Figure 1B, it is reduced to roughly one-half the 617 cm^{-1} peak value, followed by a further decrease in Figure 1C. Figure 1A is similar to results reported by Linevsky,[3] who deposited sample and recorded the spectrum of Xe/LiF at about 4.2 K. Figure 1B is similar to results reported by Snelson and Pitzer,[4] who used liquid H_2 coolant (20 K) instead of liquid He. In contrast with the relatively steady IR absorbance of the 617 cm^{-1} B_{3u} dimer peak, that for the 823 cm^{-1} monomer peak is decreased by more than two-thirds in Figure 1B and is nearly absent in Figure 1C. The 617 cm^{-1} peak is the only one in Figure 1C to plainly resemble its initial form in Figure 1A.

Figure 2 shows IRMI spectra based on Ar and Ar-mixed matrices. The top lines of Figure 1 for Xe and Figure 2 for Ar provide references for comparing the effects of matrix annealing, warming, and disordering treatments on the monomer and rhombic dimer spectral transitions. Warm-up of the Ar matrix samples destabilizes the trapping sites to produce a significant

† Part of the "Robert W. Field Festschrift".

10.1021/jp903816n CCC: $40.75
Published on Web 07/01/2009

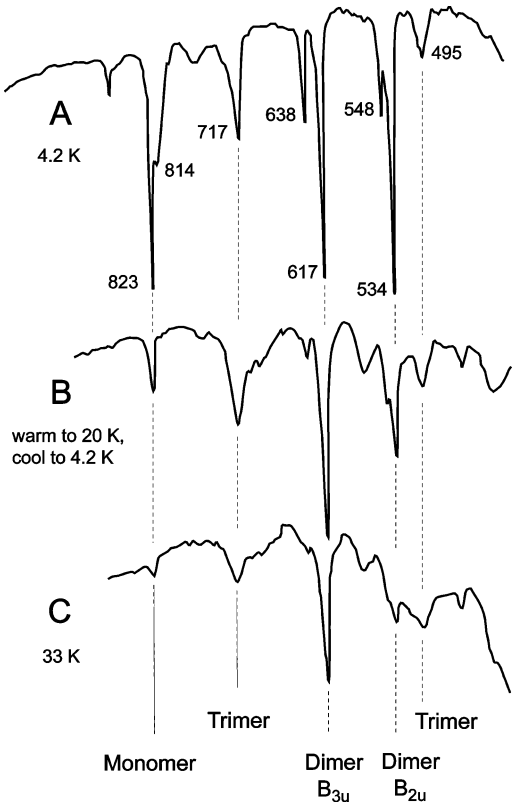

Figure 1. IR absorption spectra (cm^{-1}) of LiF species isolated in Xe with matrix/sample = 500. (A) Sample deposited and recorded at a nominal 4.2 K. (B) Sample A after warming to 20 K and cooling back to 4.2 K. (C) Warm-up of sample B with recording at 33 K.

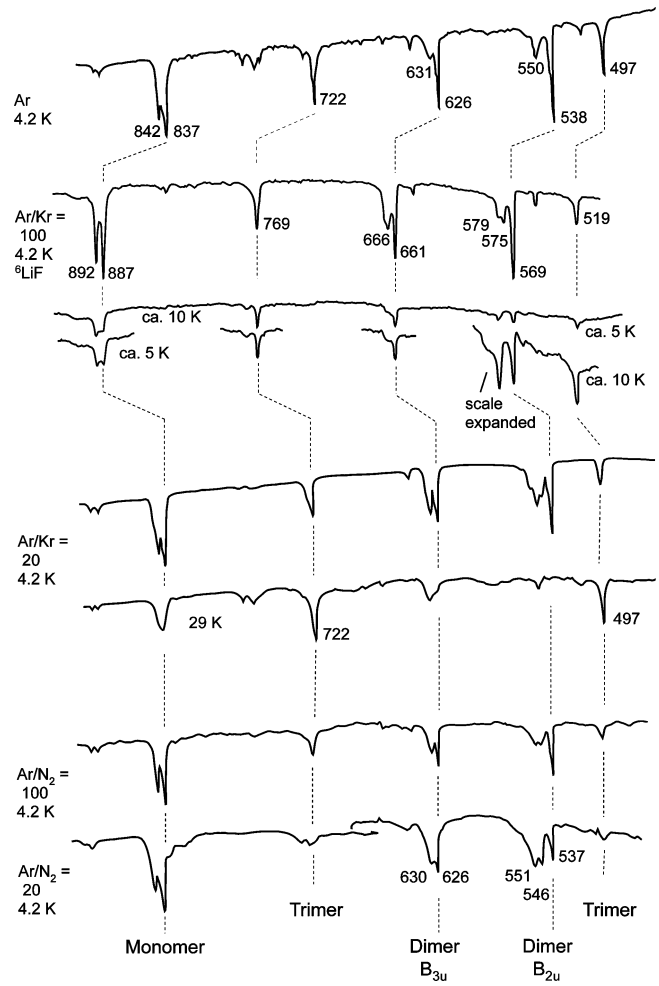

Figure 2. IR absorption spectra (cm^{-1}) of LiF species isolated in Ar and in Ar-mixed matrices with the sample depositions at a nominal 4.2 K. Warm-up behavior is shown for the Ar/Kr = 100 (^{6}LiF) and Ar/Kr = 20 samples. They were warmed to about 25 K before recording the spectra at the indicated temperatures.

decrease of the isolated sample quantities and spectral qualities,[2−12] while in Ar-mixed matrices perturbed matrix trapping sites are formed during the low temperature matrix deposition. The Ar/Kr lines in Figure 2 (Ar/Kr = 100, with 95.7% ^{6}Li enrichment, and Ar/Kr = 20 with 92.6% normal ^{7}Li abundance) show the strong rg-induced red shift and doubling of the fundamental transition of the LiF monomer. The ^{7}LiF fundamental is red-shifted from its 896.0 gas phase origin[21] to 842 and 837 cm^{-1} in Ar matrix isolation (−56 cm^{-1}, −6.3%) with absorbance $Abs_{842} < Abs_{837}$. The doublet components degrade together during annealing and warming treatments given the neat Ar matrix[2−12] and in Ar-mixed matrices such as shown in Figure 2. During most of its lifetime as an Ar-isolated species, the LiF monomer appears to be preserved in roughly its originally deposited site configurations. In contrast, Figure 1 suggests that in the larger Xe vacancy the LiF monomer is labile. Annealing transfers the metastable secondary LiF population responsible for the 814 cm^{-1} transition to the primary site population responsible for the 823 cm^{-1} transition. The strong decline of 823 cm^{-1} absorbance parallels that of the 534 cm^{-1} dimer peak, and the monomer and dimer are equally liable to the special behavior described below for the dimer. This dynamical behavior—as well as normal diffusion from the trapping site to form higher oligomers—is likely to contribute to the marked decline of IR absorbance by the 823 cm^{-1} monomer peak in Figure 1.

Figure 1A shows that the intense 617 and 534 cm^{-1} peaks of the rhombic dimer are accompanied by weaker absorptions at 638 and 548 cm^{-1}. The IR absorbance behavior of the latter peaks parallels that of the 814 cm^{-1} monomer peak to suggest that the dimer, as well as the monomer, is easily driven from metastable secondary Xe trapping sites. The Ar-mixed matrices in Figure 2 produce dimer peaks from the secondary sites that are much more intense than those observed for the pure Ar matrix. This probably reflects the integration of Li_2F_2•X units into the trapping site structures of the Ar/X mixed matrix. Similar spectra arise for $Ar/O_2 = 20$ (dimer peaks at 629, 625 and at 545, 537 cm^{-1}) and $Ar/CH_4 = 20$ (dimer peaks at 626, ∼629 sh and at 544, 537 cm^{-1}). The spectra obtained for LiF and Li_2F_2 isolated in Ar and Ar-mixed matrices show little evidence for parallels to the distinctive relative IR absorbance changes seen in Figure 1 for the Xe matrix.

4. Trapping Sites

The IRMI spectra are addressed by assuming ideal ss Xe and Ar sites in the fcc matrix crystallites. Figure 3A illustrates one of the 24 energetically equivalent tetragonal sites that can be visited through rotations of Li_2F_2 (with distinguishable atoms) in the ideal nn cluster. The site energy is labeled E_{tet}. Figure 3B illustrates one of 48 energetically equivalent trigonal sites that can be visited through rotations of Li_2F_2. In these sites, the F···F axis lies in a hexagonal plane and the Li···Li axis is on a diagonal connecting opposite corners of the nn guide cube. Each Li atom thereby has strong contacts with three Xe or Ar atoms. This site energy is labeled $E_{trig\text{-}Li}$. In a second set of 48 configurations, the Li···Li axis lies in a hexagonal plane and

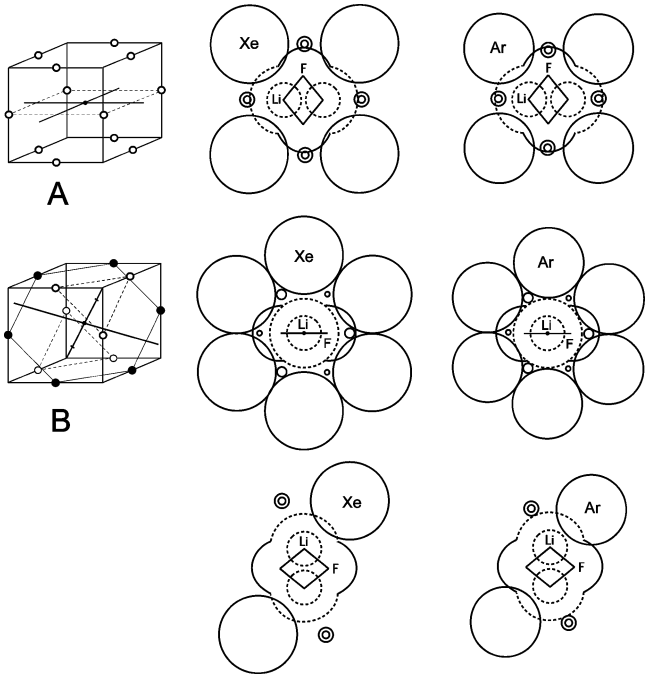

Figure 3. (A) Li_2F_2 in a tetragonal (tet) ss vacancy based on the ideal 12-atom nn cluster of the fcc lattice. There are 24 energetically equivalent configurations with the Li···Li and F···F axes directed between rg tetrads. Standard atomic van der Waals diameters[22] provide an upper limit for the Li_2F_2 size. The smaller circle on Li shows a more realistic approximation for $Li^{\delta+}$ (see text). The F^- diameter (not drawn) just eliminates the overlap between F and Xe. Small circles locate axes piercing rg atoms above and below the Li_2F_2 plane. (B) Li_2F_2 in a trigonal (trig-Li) configuration. There are 48 energetically equivalent configurations with F···F in a hexagonal plane and Li···Li on a diagonal connecting opposite corners of the guide cube. Use of the standard F^- ion diameter[22] reduces the overlap between F and Xe atoms by only about one-quarter to suggest some strain on the ideal trapping site. The lower drawings show a cross-section of the site in the plane of Li_2F_2. Here, small circles locate axes piercing out-of-plane atoms of the Xe_3 and Ar_3 triads.

the F···F axis is on a cube diagonal. The energy for these critical point configurations is labeled $E_{trig\text{-}F}$.

Guest−host size compatibilities are considered in Figure 3. First, the standard atomic van der Waals diameters[22] $D_{Xe} = 4.32$, $D_{Ar} = 3.76$, $D_{Li} = 3.64$, and $D_F = 2.94$ Å are used to provide an upper limit estimate for the Li_2F_2 volume. Using the ion diameter[22] $D_{F^-} = 2.66$ Å (the coordination number is 6) instead of $D_F = 2.94$ Å eliminates the overlap of F and Xe in Figure 3A and reduces that in Figure 3B by about one-quarter. The Li^+ ion diameter is strongly dependent on environment, cf. $D_{Li^+} = 1.84$, 1.52, and 1.18 Å for coordination numbers 8, 6, and 4, respectively.[22] The observed bond length for the LiF monomer[23] is $r_{LiF} = 1.564$ Å, and for Li_2F_2, it is[24,25] $r_{LiF} = 1.737 \pm 0.009$ Å ($\angle FLiF = 102 \pm 2°$). Using $D_{F^-} = 2.66$ Å with these bond lengths yields $D_{Li}{}^{\delta+} = 0.47$ for LiF and $D_{Li}{}^{\delta+} = 0.81$ Å for Li_2F_2—values much smaller than the listed crystal ion diameters. Using the 6-31G* basis set, the Li···Ar contact distances were calculated[11,26] for several complexes. Together with $D_{Ar} = 3.76$ Å,[22] they yield large $D_{Li}{}^{\delta+}$ values: (a) for linear FLi···Ar, $r_{Li\cdots Ar} = 2.69$ Å (RHF) → $D_{Li}{}^{\delta+} = 1.62$ Å, and 2.48 Å (MP2) → 1.20 Å; (b) for planar $FLi\cdots Ar_2$, 2.57 Å (MP2) → 1.38 Å; and (c) for $Ar_2\cdots LiF_2Li\cdots Ar_2$ (D_{2h}, with in-plane Li and Ar atoms), 2.98 Å (RHF) → 2.20 Å. The latter entity roughly superposes atoms of the ideal trig-F site, where Li···Ar is 2.85 Å.

The value $D_{Li}{}^{\delta+} = D_{Li^+}(CN = 8) = 1.84$ Å is drawn in Figure 3 as a pragmatic reference diameter for describing the "soft" Li···rg van der Waals contacts of Li_2F_2. This boundary is intended to signify a loose fit of Li···Li into Xe sites, while retaining appreciable coupling between $Li^{\delta+}$ and the Xe_3 triads. The polar Li−F bond is predominantly ionic in character,[27] but the Li atoms in LiF and its low oligomers all carry computed charges that are less than +1 (cf. +0.55e for Li in LiF)[27] to suggest a rationale for the widely dispersed $D_{Li}{}^{\delta+}$ values.

TABLE 1: Li_2F_2 Contacts in Xe ss Trapping Sites

interaction	tet	trig-Li	trig-F
F···Xe (repulsive)	8	4	6
Li···Xe (attractive)	8	6	4
attractive−repulsive	0	2	−2

Table 1 characterizes the three sets of trapping site PES critical point configurations by classing the nn Li···Xe overlaps as attractive and the nn F···Xe overlaps as repulsive. With the IRMI observations indicating the presence of primary and secondary trapping site minima, the critical point configurations are ranked as $E_{trig\text{-}Li}$ (primary minimum) < E_{tet} (secondary minimum) < $E_{trig\text{-}F}$ (maximum). A positive energy difference was computed[26] for $Ar_{12}Li_2F_2$ at the MP2/6-311++G(2d) level using the $r_{Ar\cdots Ar}$ distance 3.77 Å: $E_{trig\text{-}F} - E_{trig\text{-}Li} = -6538.2821 + 6538.2916 = +0.0095$ H, e.g., ∼6 kcal/mol. The computed energy minimum for $E_{trig\text{-}Li}$ occurs for $r_{Ar\cdots Ar} > 4$ Å. Figure 3 suggests that the minimum energy pathways between $E_{trig\text{-}Li}$ configurations in different hexagonal planes pass through an E_{tet} configuration (and vice versa). Both the primary $E_{trig\text{-}Li}$ and the secondary E_{tet} site configurations are populated during the Xe, Ar, and Ar-mixed matrix depositions. However, only the looser fit and lower PES barriers of the Xe matrix sites provide conditions conducive to rotational stereodynamics—at an onset temperature between 4.2 and 20 K. The CN radical is observed to show nearly free rotation in Xe matrix isolation.[18] Its bond length is $r_{CN} = 1.172$ Å,[28] and the atomic van der Waals diameters[22] are $D_C = 3.40$ and $D_N = 3.10$ Å. These yield 4.42 Å as the estimated length for the CN molecule, to be compared with $D_{Xe} = 4.32$ A.

5. Induced Transparency of the 534 cm^{-1} B_{2u} Mode

Figure 4 shows normal coordinates approximated using quantum chemistry[12] for the B_{3u}, B_{2u}, and B_{1u} fundamentals of Li_2F_2. With Li_2F_2 isolated in trig-Li site configurations (Figure 3B), the B_{2u} mode excitation sends the Li atoms directly into triads of Xe atoms. In this setting, a cumulative vibrational relaxation mechanism that spreads from 534 cm^{-1} B_{2u} to Xe crystallite modes to Li_2F_2 librations can credibly induce rotational stereodynamics activity. The IR absorbances in Figure 1 clearly show that the requisite couplings occur for only one dimer mode—534 cm^{-1} B_{2u}. Molecular dynamics computations[29,30] performed to elucidate isomerization experiments on matrix-isolated HONO also embody the present kindred situation. The computations produce vibrational specificity and a relaxation

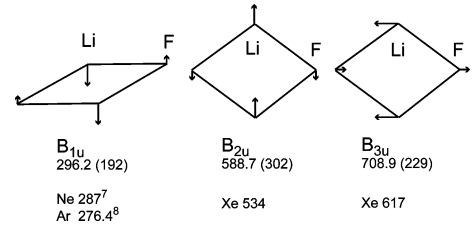

Figure 4. Normal coordinates for Li_2F_2 as estimated using quantum chemistry at the MP2/6-31* level.[12] Frequencies are in cm^{-1}, and intensities are in kM/mol.

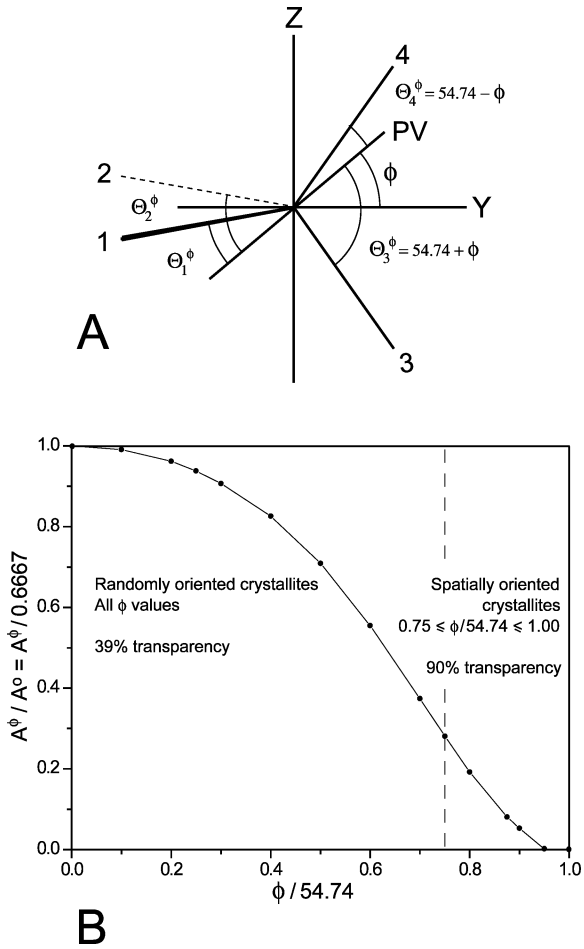

Figure 5. (A) Diagram illustrating the tetrahedral orientations, arms 1−4, taken by the collective transition dipoles of the 534 cm^{-1} B_{2u} mode of Li_2F_2 isolated in trig-Li configurations of rg crystallites. Arms 3, 4, and line PV (which is collinear with the IR propagation vector) lie in the YZ plane. Arms 1 and 2 lie in the XY plane above and below the YZ plane, respectively. In this figure, the transition dipoles are space-fixed, and line PV is rotated in the YZ plane through the range $0 \leq \phi \leq 54.74$ to sample effects of the crystallite orientation relative to the IR propagation vector. The Θ_i^{ϕ} angles determine the perpendicular and parallel components of the transition dipoles relative to the PV line. (B) Graph showing the calculated ø-dependent relative IR absorbance by the collected B_{2u} transition dipoles of Xe-isolated Li_2F_2 (see the text and Figure 5A).

mechanism that couples HONO vibrational states to Xe or Ar lattice vibrations to HONO rotation to HONO torsional isomerization.

Rotational stereodynamics shifts Li_2F_2 between the (ideally) 48 PES minima of the trig-Li site configurations. When Li_2F_2 lands in a site that roughly aligns the transition dipole (the Li···Li axis) with the IR propagation vector, the ability of Li_2F_2 to absorb 534 cm^{-1} radiation is reduced. Furthermore, with perfect alignment, the Li_2F_2 cannot leave the site because (a) it is then transparent to 534 cm^{-1} radiation and (b) the excitation of other vibrations does not produce rotational stereodynamics.

Figure 3B shows that four distinct hexagonal planes pass through the origin of a ss rg vacancy. Each plane is normal to a diagonal connecting opposite corners of the guide cube. In trig-Li configurations, the Li···Li axis and the B_{2u} transition dipole lie on these same diagonals, which are represented by arms 1−4 in Figure 5A. The B_{2u} transition dipoles for a set of Li_2F_2 molecules isolated in a single rg crystallite are therefore dispersed among four spatial orientations. The B_{2u} dipoles present in the numerous crystallites comprising a matrix sample are randomly oriented in space insofar as the crystallites have random spatial orientations. The spatial orientations of a crystallite relative to the propagation vector of the IR beam are sampled as illustrated in Figure 5A. The IR propagation vector, collinear with line PV, is rotated through an angle ø in the YZ plane. With arm 4 chosen as being the one most nearly collinear with line PV, the ø range is $0 \leq \text{ø} \leq 54.74°$. Angles $\Theta_1^{\text{ø}}$ to $\Theta_4^{\text{ø}}$ give the offsets between PV and the four transition dipole vectors.

IR absorbance by each of the four transition dipole orientations derives from the vector component lying perpendicular to the propagation vector. Taking the constant multiplier as unity, the relative IR absorbances $a_i^{\text{ø}}$ ($i = 1-4$) for the transition dipole orientations are $a_i^{\text{ø}} = \sin^2 \Theta_i^{\text{ø}}$. Equations giving the ø-dependent relative equilibrium populations $n_i^{\text{ø}}$ are

$$-a_1^{\text{ø}}n_1^{\text{ø}} + 1/3a_2^{\text{ø}}n_2^{\text{ø}} + 1/3a_3^{\text{ø}}n_3^{\text{ø}} + 1/3a_4^{\text{ø}}n_4^{\text{ø}} = 0 \quad (1)$$

$$+1/3a_1^{\text{ø}}n_1^{\text{ø}} - a_2^{\text{ø}}n_2^{\text{ø}} + 1/3a_3^{\text{ø}}n_3^{\text{ø}} + 1/3a_4^{\text{ø}}n_4^{\text{ø}} = 0 \quad (2)$$

$$+1/3a_1^{\text{ø}}n_1^{\text{ø}} + 1/3a_2^{\text{ø}}n_2^{\text{ø}} - a_3^{\text{ø}}n_3^{\text{ø}} + 1/3a_4^{\text{ø}}n_4^{\text{ø}} = 0 \quad (3)$$

$$+1/3a_1^{\text{ø}}n_1^{\text{ø}} + 1/3a_2^{\text{ø}}n_2^{\text{ø}} + 1/3a_3^{\text{ø}}n_3^{\text{ø}} - a_4^{\text{ø}}n_4^{\text{ø}} = 0 \quad (4)$$

In eq 1, the $-a_1^{\text{ø}}n_1^{\text{ø}}$ term expresses the rate that population leaves arm 1 and the other three terms express the rates that arm 1 receives its statistical share, 1/3, of the populations exiting arms 2, 3, and 4. The $a_i^{\text{ø}} = \sin^2 \Theta_i^{\text{ø}}$ values follow the choice for ø (cf. Figure 5A) and the simultaneous solution of eqs 1−4 for arms 1−4 yields the four relative equilibrium $n_i^{\text{ø}}$ values. These are observable quantities insofar as the rate of rotational stereodynamics is fast on the time scale of the classical IRMI experiments. The ø dependence of the total relative IR absorbance is expressed as $A^{\text{ø}} = \Sigma n_i^{\text{ø}} a_i^{\text{ø}}$.

At ø = 0, each of the four Θ_i^0 values is 54.74° to yield $a_i^{\text{ø}} = a_i^0 = 0.6667$. A simultaneous solution of eqs 1−4 then produces $n_i^0 = 0.25$ (subject to $\Sigma n_i^{\text{ø}} = 1$) and $A^{\text{ø}} = A^0 = \Sigma n_i^0 a_i^0 = 0.6667$. At ø = 0, there is no induced transparency: $A^{\text{ø}}/A^0 = 1$. Figure 5A shows that at $\text{ø} = 54.74°$, $\Theta_1^{54.74} = \Theta_2^{54.74} = 109.48°$, $\Theta_3^{54.74} = 109.48°$, and $\Theta_4^{54.74} = 0°$ to produce from eqs 1−4 the relative equilibrium populations $n_1^{54.74} = n_2^{54.74} = n_3^{54.74} = 0$ and $n_4^{54.74} = 1$. With all of the Li_2F_2 molecules oriented in arm 4—the transparent configuration—$A^{54.74} = 0$: that is, $A^{54.74}/A^0 = 0$. In Figure 5B, the absorbance ratio $A^{\text{ø}}/A^0 = \Sigma n_i^{\text{ø}} a_i^{\text{ø}}/0.6667$ is plotted as a function of ø/54.74. The integral over ø shows that at equilibrium the induced transparency effect of the rotational stereodynamics causes a decrease of absorbance at 534 cm^{-1} by more than one-third. The defined model thus predicts an appreciable induced IR transparency for completely random Xe crystallite orientations (i.e., the taking of all ø values as equally probable).

Experimental evidence shows that for some matrix-isolated substances the matrix crystallites situate guest molecules with preferred spatial orientations, cf. the discussion and the observations of Xe-isolated SF_6 by Jones et al.[31] In the present case, the transparency to 534 cm^{-1} radiation is increased if there is a tendency for the Xe crystallites to become oriented during the deposition (or afterward) with a hexagonal plane roughly paralleling the cold deposition window. Figure 5B shows that

limiting ø to the range $0.75 \leq ø/54.74 \leq 1.00$ reduces the 534 cm^{-1} absorbance integral to 10% (i.e., 90% transparency). Snelson[32] noted IR evidence for spatially oriented AlF_3 and, possibly, Li_2F_2 in Ar matrix isolation experiments. Fajardo and Lindsay[33] used a new state-of-art polarized infrared absorption spectroscopy (PIRAS) apparatus to show that for the case of water doped into solid para hydrogen there is a strong alignment between the *c*-axis of the hcp cystallites of pH_2 and the normal to the deposition substrate (a cold mirror).

6. Concluding Remarks

1. Signaling the presence of vibrational state-specific induced rotational stereodynamics by Li_2F_2 in Xe matrix trapping sites, IR absorbance by the 534 cm^{-1} B_{2u} fundamental is markedly decreased under conditions that only moderately affect absorbance by the 617 cm^{-1} B_{3u} fundamental. The phenomenon is attributed to rotational stereodynamics released by the vibrational relaxation mechanism of the 534 cm^{-1} B_{2u} excitation, which is postulated to couple the Li_2F_2 vibration to Xe crystallite vibrations to Li_2F_2 librational motions. PES barriers retarding the movement of Li_2F_2 among the trig-Li configurations are overcome at some temperature, $4.2 < T < 20$ K, where the rotational stereodynamics becomes fast on the time scale of the classical IRMI experiment. The Li_2F_2 collects, through lack of an escape route, in trig-Li trapping site configurations showing transparency to 534 cm^{-1} radiation because they provide an approximate alignment between the B_{2u} transition dipole (the Li···Li axis) and the propagation vector of the spectrometer IR beam. The large absorbance decreases shown by the 534 cm^{-1} B_{2u} dimer peak and the 823 cm^{-1} monomer peak, relative to the 617 cm^{-1} B_{3u} dimer peak, also argue that the Xe matrix crystallites may, to some degree, be spatially oriented to favor rough coplanarity of a hexagonal plane and the matrix deposition window. Observations showing evidence for spatially oriented matrix crystallites have been reported.[31−33]

2. The observed IR absorbance behavior follows from size-symmetry considerations of the ideal guest−host system. The PES for the postulated ideal ss fcc Xe sites hosting Li_2F_2 (D_{2h}) is highly dimpled, and in primary site configurations, the Li···Li axis coincides with one of four trigonal site axes connecting opposite corners of the nn guide cube. Strong interactions between Li and the adjoining Xe triads stabilize the sites and foment the proposed state-specific vibrational relaxation behavior of the 534 cm^{-1} B_{2u} fundamental. The Xe-isolated LiF monomer also occupies the generic trigonal primary sites, thereby allowing its dynamical-spectroscopic behavior to parallel that of the B_{2u} dimer mode. Figure 3 clearly shows that the compatible size-symmetry conditions holding for Xe-isolated Li_2F_2 are strained in Ar. However, the IRMI spectra for Xe, Ar, and Ar-mixed matrices suggest that the basic trapping site configurations defined by the Xe matrix carry through, with distortion, for those of Ar.

3. The described rotational stereodynamics phenomenon increases the Abs_{617}/Abs_{534} IR absorbance ratio through the reduction of Abs_{534} with concomitant enhancement of Abs_{617}. The effect is clear in Figure 1; however, the spectra also include the consequences of the net Li_2F_2 population decrease that accompanies guest species diffusions in a warming matrix. The prominent 617 cm^{-1} absorbance in Figures 1A−C suggests that the increase in Abs_{617} obtained through rotational stereodynamics and through relaxation of Li_2F_2 from the tet site to the trig-Li site is able to compensate much of the Abs_{617} decrease attributable to the diffusional loss of Li_2F_2 population in trig-Li sites. The present report demonstrates the presence of novel dynamical behavior in the Xe/LiF system resulting from grossly different vibrational relaxation processes by the 534 cm^{-1} B_{2u} and 617 cm^{-1} B_{3u} fundamentals. Subsequent experiments should include systematic variations of selected experimental parameters and the monitoring of species populations through integrated IR absorbances. Kinetics measurements would be particularly appropriate, along with first spectroscopic studies of the B_{1u} IR mode of Xe/Li_2F_2 and of the three gerade fundamentals of Li_2F_2.

Acknowledgment. This article is dedicated to Prof. Robert W. Field. I am grateful to T. E. Redington for her contributions to the work and to the U.S. Army Research Office (Durham) and the Robert A. Welch Foundation for their past support of the infrared laboratory and matrix-isolation research program.

References and Notes

(1) Hargittai, M. *Chem. Rev.* **2000**, *100*, 2233.
(2) Linevsky, M. J. *J. Chem. Phys.* **1961**, *34*, 587.
(3) Linevsky, M. J. *J. Chem. Phys.* **1963**, *38*, 658.
(4) Snelson, A.; Pitzer, K. S. *J. Phys. Chem.* **1963**, *67*, 882.
(5) Schlick, S.; Schnepp, O. *J. Chem. Phys.* **1964**, *41*, 463.
(6) Redington, R. L. *J. Chem. Phys.* **1966**, *44*, 1238.
(7) Snelson, A. *J. Chem. Phys.* **1967**, *46*, 3652.
(8) Abramowitz, S.; Acquista, N.; Levin, I. W. *J. Res. Natl. Bur. Stand.* **1968**, *72A*, 487.
(9) Martin, T. P. *Phys. Rev. B* **1977**, *15*, 4071.
(10) Ramondo, F.; Bencivenni, L.; Rossi, F. *Chem. Phys.* **1988**, *124*, 291.
(11) Redington, R. L. *J. Chem. Phys.* **1995**, *102*, 7325.
(12) Redington, R. L. *J. Chem. Phys.* **1995**, *102*, 7332.
(13) Haas, Y.; Samuni, U. *Prog. React. Kinet.* **1998**, *23*, 211.
(14) Anderson, D. T.; Winn, J. S. *Chem. Phys.* **1994**, *189*, 171.
(15) Pardanaud, C.; Vasserot, A.-M.; Michaut, X.; Abouaf-Marguin, L. *J. Mol. Struct.* **2008**, *873*, 181.
(16) Jacox, M. E.; Thompson, W. E. *J. Mol. Spectrosc.* **2004**, *228*, 414.
(17) Jones, L. G.; Ekberg, S. A.; Swanson, B. I. *J. Chem. Phys.* **1986**, *85*, 3203.
(18) Schallmoser, G.; Thoma, A.; Wurfel, B. E.; Bondybey, V. E. *Chem. Phys. Lett.* **1994**, *219*, 101.
(19) Maçôas, E. M. S.; Khriachtchev, L.; Pettersson, M.; Fausto, R.; Räsänen, M. *J. Chem. Phys.* **2004**, *121*, 1331.
(20) Varetti, E. L.; Pimentel, G. C. *J. Chem. Phys.* **1971**, *55*, 3813.
(21) Hedderich, H. G.; Frum, C. I.; Englemen, R.; Bernath, P. F. *Can. J. Chem.* **1991**, *69*, 1659.
(22) Lide, D. R., Ed. *Handbook of Chemistry and Physics*, 89th ed.; CRC Press: New York, 2008−2009.
(23) Wharton, L.; Klemperer, W.; Gold, L. P.; Stauch, R.; Gallagher, J. J.; Derr, V. E. *J. Chem. Phys.* **1963**, *38*, 1203.
(24) Solomonik, V. G.; Krasnov, K. S.; Girichev, G. V.; Zasorin, E. Z. *J. Struct. Chem.* **1979**, *20*, 361.
(25) Lapshina, S. B.; Girichev, G. V. *J. Struct. Chem.* **1991**, *32*, 48.
(26) Frisch, M. J.; Trucks, G. W.; Schlegel, H. B.; Scuseria, G. E.; Robb, M. A.; Cheeseman, J. R.; Zakrzewski, V. G.; Montgomery, J. A., Jr.; Stratmann, R. E.; Burant, J. C.; Dapprich, S.; Millam, J. M.; Daniels, A. D.; Kudin, K. N.; Strain, M. C.; Farkas, O.; Tomasi, J.; Barone, V.; Cossi, M.; Cammi, R.; Mennucci, B.; Pomelli, C.; Adamo, C.; Clifford, S.; Ochterski, J.; Petersson, G. A.; Ayala, P. Y.; Cui, Q.; Morokuma, K.; Malick, D. K.; Rabuck, A. D.; Raghavachari, K.; Foresman, J. B.; Cioslowski, J.; Ortiz, J. V.; Stefanov, B. B.; Liu, G.; Liashenko, A.; Piskorz, P.; Komaromi, I.; Gomperts, R.; Martin, R. L.; Fox, D. J.; Keith, T.; Al-Laham, M. A.; Peng, C. Y.; Nanayakkara, A.; Gonzalez, C.; Challacombe, M.; Gill, P. M. W.; Johnson, B. G.; Chen, W.; Wong, M. W.; Andres, J. L.; Head-Gordon, M.; Replogle, E. S.; Pople, J. A. Gaussian 98, revision A.6; Gaussian, Inc.: Pittsburgh, PA, 1998.
(27) Bickelhaupt, F. M.; Solà, M.; Fonseca Guerra, C. *J. Comput. Chem.* **2007**, *28*, 238.
(28) Prasad, C. V. V.; Bernath, P. F.; Frum, C.; Engleman, R. J., Jr. *Mol. Spectrosc.* **1992**, *151*, 459.
(29) Agrawal, P. M.; Thompson, D. L.; Raff, L. M. *J. Chem. Phys.* **1994**, *101*, 9937.
(30) Agrawal, P. M.; Thompson, D. L.; Raff, L. M. *J. Chem. Phys.* **1995**, *102*, 7000.
(31) Jones, L. H.; Swanson, B. I.; Fry, H. A. *Chem. Phys. Lett.* **1982**, *87*, 397.
(32) Snelson, A. *J. Phys. Chem.* **1967**, *71*, 3202.
(33) Fajardo, M. E.; Lindsay, C. M. *J. Chem. Phys.* **2008**, *128*, 014505.

JP903816N